JOURNAL OF COMPUTATIONAL PHYSICS 117, 274–280 (1995)

Quantum Hydrodynamic Simulation of Hysteresis in the Resonant Tunneling Diode

ZHANGXIN CHEN*

Department of Mathematics and Institute for Scientific Computation, Texas A&M University, College Station, Texas 77843

BERNARDO COCKBURN†

School of Mathematics, University of Minnesota, Minneapolis, Minnesota 55455

CARL L. GARDNER‡

Department of Computer Science and Department of Mathematics, Duke University, Durham, North Carolina 27706

AND

JOSEPH W. JEROME§

Department of Mathematics, Northwestern University, Evanston, Illinois 60208

Received March 25, 1994; revised August 8, 1994

Hysteresis in the current–voltage curve of a resonant tunneling diode is simulated and analyzed in the quantum hydrodynamic (QHD) model for semiconductor devices. The simulations are the first to show hysteresis in the QHD equations and to confirm that bistability is an intrinsic property of the resonant tunneling diode. Hysteresis appears in many settings in fluid dynamics. The simulations presented here show that hysteresis is manifested in the extension of classical fluid dynamics to quantum fluid dynamics. A finite element method for simulation of the time-dependent QHD model is introduced. The finite element method is based on a Runge–Kutta discontinuous Galerkin method for the QHD conservation laws and a mixed finite element method for Poisson's equation and the source terms in the QHD conservation laws. © 1995 Academic Press, Inc.

1. INTRODUCTION

The quantum hydrodynamic (QHD) model approximates quantum effects in the propagation of electrons in a semiconductor device by adding quantum corrections to the classical hydrodynamic equations. The leading $O(\hbar^2)$ quantum corrections have been remarkably successful in simulating the effects of electron tunneling through potential barriers including single [1, 2] and multiple [3] regions of negative differential resistance in the current–voltage curves of resonant tunneling diodes.

There are three major advantages of using the quantum hydrodynamic model over other methods for simulating quantum semiconductor devices. First, the QHD method is much less computationally intensive than the Wigner function [4] or density matrix [5] methods, and includes the same physics if the expansion parameter $\hbar^2/8mTl^2$ is small. Second, the QHD equations are expressed in terms of intuitive classical fluid dynamical quantities (e.g., density, velocity, and temperature). Third, well-understood classical boundary conditions can be imposed in simulating quantum devices.

Intrinsic bistability (as opposed to extrinsic bistability, which is due to the coupling of the resonant tunneling diode to an external circuit) in the measured current–voltage curves of double barrier resonant tunneling diodes has been reported by various experimental groups (see Ref. [6]). In this investigation, we present QHD simulations of hysteresis in a GaAs/$Al_xGa_{1-x}As$ double barrier resonant tunneling diode at 77 K. These are the first simulations of the QHD equations to show hysteresis. The simulations demonstrate that bistability is an intrinsic property of the resonant tunneling diode, in agreement with simulations of the Wigner–Boltzmann equation [4].

Thus the simulations presented here show that the $O(\hbar^2)$

* Research supported in part by the Department of Energy under Grant DE-AC05-840R21400 and by the U.S. Army Research Office under Grant DAAL03-89-C-0038 with the University of Minnesota Army High Performance Computing Research Center.

† Research supported in part by the National Science Foundation under Grant DMS-9103997 and by the Minnesota Supercomputer Institute.

‡ Research supported in part by the U.S. Army Research Office under Grant DAAL03-91-G-0146 and by the National Science Foundation under Grant DMS-9204189.

§ Research supported in part by the National Science Foundation under Grant DMS-9123208.

0021-9991/95 $6.00
Copyright © 1995 by Academic Press, Inc.
All rights of reproduction in any form reserved.

QHD equations reproduce important features of solutions to the full Wigner–Boltzmann equation and that hysteresis occurs in the extension of classical fluid dynamics to quantum fluid dynamics.

We introduce a finite element method for simulating the time-dependent QHD model, which generalizes a method successfully applied to two-dimensional classical hydrodynamic simulations of a MESFET [7]. The finite element method is based on a Runge–Kutta discontinuous Galerkin method for the QHD conservation laws and a mixed finite element method for Poisson's equation and the source terms in the QHD conservation laws.

Points on the current–voltage curve are obtained by integrating the time-dependent QHD equations to steady state.

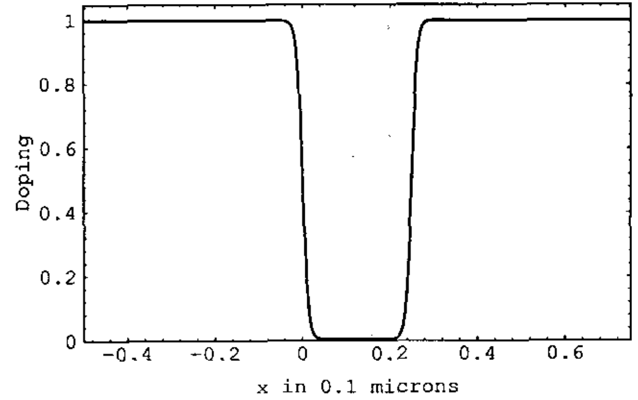

FIG. 1. Doping/10^{18} cm^{-3} and location of potential barriers (shaded gray).

2. THE QUANTUM HYDRODYNAMIC MODEL

The QHD model has exactly the same structure [2] as the classical hydrodynamic model (electrogasdynamics):

$$\frac{\partial n}{\partial t} + \frac{\partial}{\partial x_i}(nu_i) = 0 \tag{1}$$

$$\frac{\partial}{\partial t}(mnu_j) + \frac{\partial}{\partial x_i}(u_i mnu_j - P_{ij}) = -n\frac{\partial V}{\partial x_j} - \frac{mnu_j}{\tau_p} \tag{2}$$

$$\frac{\partial W}{\partial t} + \frac{\partial}{\partial x_i}(u_i W - u_j P_{ij} + q_i) = -nu_i\frac{\partial V}{\partial x_i} - \frac{(W - (3/2)nT_0)}{\tau_w} \tag{3}$$

$$\nabla \cdot (\varepsilon \nabla V) = e^2(N_D - N_A - n), \tag{4}$$

where n is the electron density, $\mathbf{u}$ is the velocity, m is the effective electron mass, P_{ij} is the stress tensor, $V = -e\phi$ is the potential energy, ϕ is the electric potential, $e > 0$ is the electronic charge, W is the energy density, $\mathbf{q}$ is the heat flux, T_0 is the temperature of the semiconductor lattice in energy units (k_B is set equal to 1), ε is the dielectric constant, N_D is the density of donors, and N_A is the density of acceptors. Spatial indices i, j equal 1, 2, 3, and repeated indices are summed over. The transport equations (1)–(3) express conservation of electron number, momentum, and energy, respectively, and Eq. (4) is Poisson's equation. The classical collision terms in Eqs. (2) and (3) are modeled by the relaxation time approximation, with momentum and energy relaxation times τ_p and τ_w. The heat flux is specified by Fourier's law $\mathbf{q} = -\kappa\nabla T$, where T is the electron temperature.

Quantum mechanical effects appear in the stress tensor and the energy density. Reference [2] derives the stress tensor and the energy density for the $O(\hbar^2)$ momentum-shifted thermal equilibrium Wigner distribution function [8]:

$$P_{ij} = -nT\delta_{ij} + \frac{\hbar^2 n}{12m}\frac{\partial^2}{\partial x_i \partial x_j}\log(n) + O(\hbar^4) \tag{5}$$

$$W = \tfrac{3}{2}nT + \tfrac{1}{2}mnu^2 - \frac{\hbar^2 n}{24m}\nabla^2 \log(n) + O(\hbar^4). \tag{6}$$

Ancona, Iafrate, and Tiersten [9, 10] derived expression (5) for the stress tensor. In Ref. [1], Grubin and Kreskovsky formulated a one-dimensional version of the QHD equations.

The expansion parameter in the asymptotic series (5) and (6) is actually $\hbar^2/8mTl^2$, where l is a characteristic length scale of the problem [10, 11]. For the resonant tunneling diode in Section 3 with $T \approx T_0 = 77$ K and $l = 100$ Å, the expansion parameter ≈ 0.23.

In one dimension, the QHD model has two Schrödinger modes, one parabolic mode, and one elliptic mode. Thus eight boundary conditions are necessary. Well-posed boundary conditions for the resonant tunneling diode are $n = N_D$, $\partial n/\partial x = 0$, and $\partial T/\partial x = 0$ at the left and right diode boundaries x_L and x_R, with a bias ΔV across the device: $V(x_L) = T\log(n/n_i)$ and $V(x_R) = T\log(n/n_i) + e\Delta V$, where n_i is the intrinsic electron concentration.

3. SIMULATIONS OF HYSTERESIS

To exhibit hysteresis, we simulate a GaAs resonant tunneling diode with double $Al_{0.3}Ga_{0.7}As$ barriers (the barrier height $\mathcal{B} = 0.209$ eV). The doping density $N_D = 10^{18}$ cm^{-3} in the n^+ source and drain, and $N_D = 5 \times 10^{15}$ cm^{-3} in the n channel (see Fig. 1). The channel is 250 Å long, the barriers are 50 Å wide, and the well between the barriers is 50 Å wide. The device has 50 Å spacers between the barriers and the contacts (source and drain) to enhance negative differential resistance.

The barrier height $\mathcal{B}$ is incorporated into the QHD transport equations (1)–(3) by the replacement $V \to V + \mathcal{B}$. Poisson's equation is not changed.

For the classical momentum and energy relaxation times, we use modified Baccarani–Wordemann models:

$$\tau_p = \tau_{p0}\frac{T_0}{T} \tag{7}$$

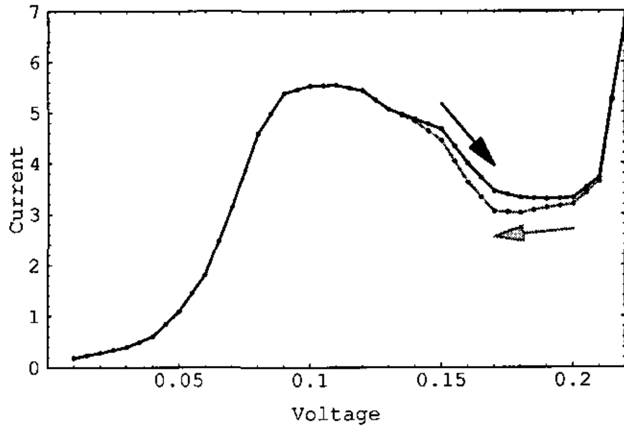

FIG. 2. Current density in kiloamps/cm² vs. voltage for the resonant tunneling diode at 77 K.

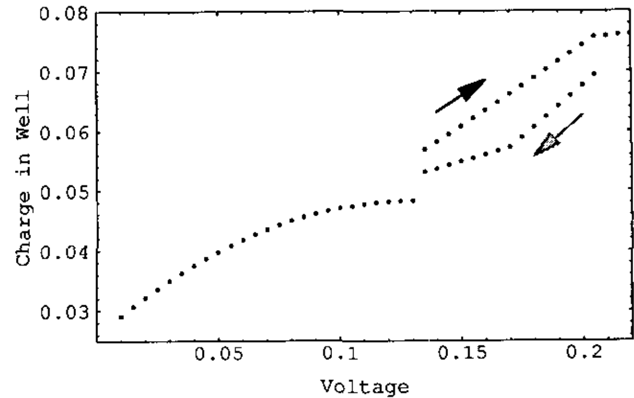

FIG. 4. Electron charge/$(-e)$ in 10^{13} cm^{-2} in the quantum well vs. voltage.

$$\tau_w = \frac{\tau_p}{2}\left(1 + \frac{(3/2)T}{(1/2)mv_s^2}\right), \tag{8}$$

where the low-energy momentum relaxation time τ_{p0} is set equal to 0.9 ps from the low-field electron mobility in GaAs at 77 K. For lower valley electrons in GaAs at 77 K, the effective electron mass $m = 0.063\ m_e$, where m_e is the electron mass, and the saturation velocity $v_s \approx 2 \times 10^7$ cm/s. κ_0 is set equal to 0.4 in the Wiedemann–Franz formula for thermal conductivity,

$$\mathbf{q} = -\kappa\nabla T, \quad \kappa = \kappa_0\tau_{p0}nT_0/m. \tag{9}$$

The dielectric constant $\varepsilon = 12.9$ for GaAs.

The current–voltage curve for the resonant tunneling diode is plotted in Fig. 2 for ΔV increasing from 0 to 0.22 V (upper curve) and decreasing from 0.22 to 0 V (lower curve). Note that hysteresis occurs predominantly in the region of negative differential resistance. The physical mechanism for hysteresis is that electrons "see" a different potential energy due to different accumulated electron charges in the diode when the applied voltage is decreasing than when the applied voltage is increasing [4]. The electron charge per area in the diode is plotted in Fig. 3. The discontinuities in electron charge at the hysteresis points are intriguing—usually the current is discontinuous at the hysteresis points—and reflect a complex underlying mathematical structure; see Golubitsky and Schaeffer [12, pp. 222–225] for a discussion of various possibilities that can occur for a "nondegenerate cubic" bifurcation problem. Figure 4 shows the electron charge per area in the quantum well, which is also discontinuous at the hysteresis points.

From the mathematical point of view, hysteresis corresponds to the existence of multiple steady states. Which steady state the computational solution converges to as $t \to \infty$ depends on the initial conditions.

When the applied voltage is decreasing in the hysteresis loop ($0.135\ \text{V} \leq \Delta V \leq 0.205\ V$), the electron density is slightly lower in the quantum well and substantially higher around the

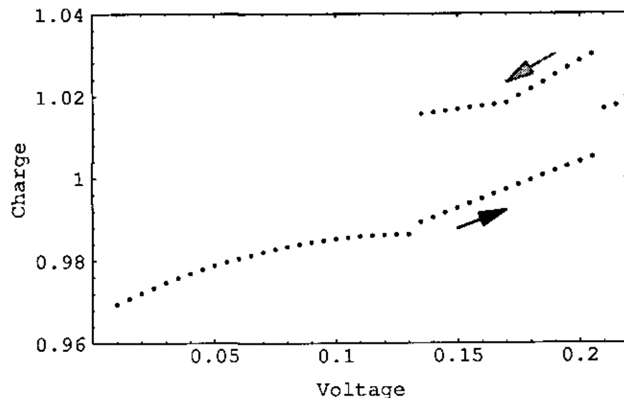

FIG. 3. Electron charge/$(-e)$ in 10^{13} cm^{-2} in the diode vs. voltage.

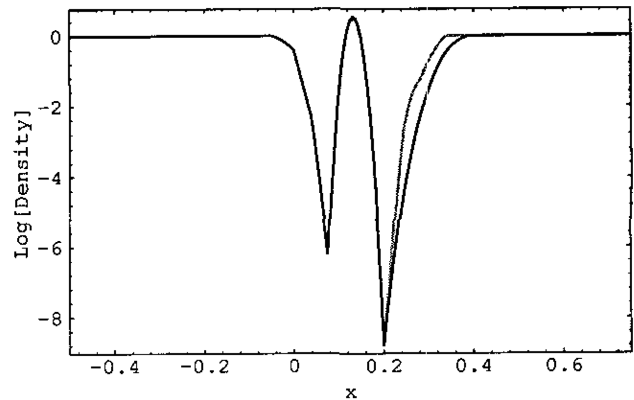

FIG. 5. Log[Density/10^{18} cm^{-3}] for $\Delta V = 0.135$ V. In this and subsequent figures, the black curve is the solution for increasing voltage and the grey curve is the solution for decreasing voltage, and x is in 0.1 μm.

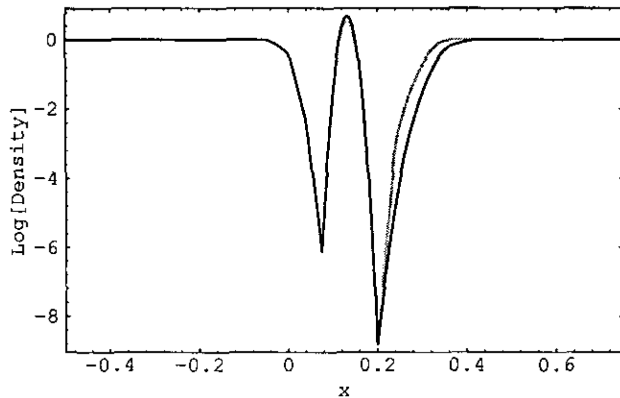

FIG. 6. Log[Density/10^{18} cm^{-3}] for $\Delta V = 0.17$ V.

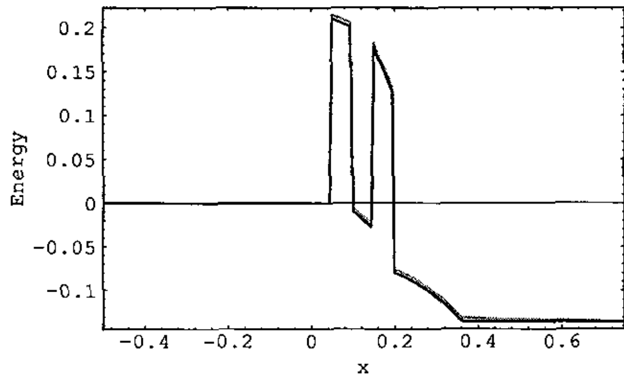

FIG. 8. Conduction band energy in eV for $\Delta V = 0.135$ V.

channel/drain junction (see Figs. 5–7). The fact that the electron charge in the well is lower for decreasing voltage implies, through Gauss' law

$$V(x) = V(x_L) + eE(x_L)(x - x_L) + \frac{e}{\varepsilon}\int_{xL}^{x} \mathcal{Q}(s)ds, \qquad (10)$$

where $\mathcal{Q}(x) = e\int_{xL}^{x}(N(s) - n(s))ds$ is the total charge per area between x_L and x and E is the electric field, that the effective potential barriers $V + \mathcal{B}$ are higher (see Figs. 8–10), thus allowing less current to flow through the device. In Eq. (10), the electric field $E = d(V/e)/dx$ vanishes at x_L for increasing voltage in the hysteresis loop and is small and positive (which also increases the effective barrier heights) for decreasing voltage (see Figs. 8–10.) The densities for increasing (decreasing) applied voltage in the hysteresis loop are almost identical, with a slight increase (decrease) in the density in the quantum well as the voltage increases (decreases).

Note also that for decreasing voltage in the hysteresis loop, the electron temperature is slightly higher in the source and the well (see Figs. 11–13).

4. NUMERICAL METHOD

We have generalized a finite element method [7], which was successfully applied to two-dimensional classical hydrodynamic simulations of a MESFET, for simulation of the time-dependent QHD model. The finite element method is based on a Runge–Kutta discontinuous Galerkin method for the QHD conservation laws and a mixed finite element method for Poisson's equation and the source terms in the QHD conservation laws.

We first rewrite the QHD transport equations (1)–(3) in a form which is identical to that of the classical hydrodynamic model with source terms:

$$\frac{\partial n}{\partial t} + \frac{\partial}{\partial x_i}(nu_i) = 0 \qquad (11)$$

$$\frac{\partial}{\partial t}(mnu_j) + \frac{\partial}{\partial x_i}(u_i mnu_j + nT\delta_{ij}) = -n\frac{\partial V}{\partial x_j} - \frac{mnu_j}{\tau_p} - \frac{n}{3}\frac{\partial Q}{\partial x_j} \qquad (12)$$

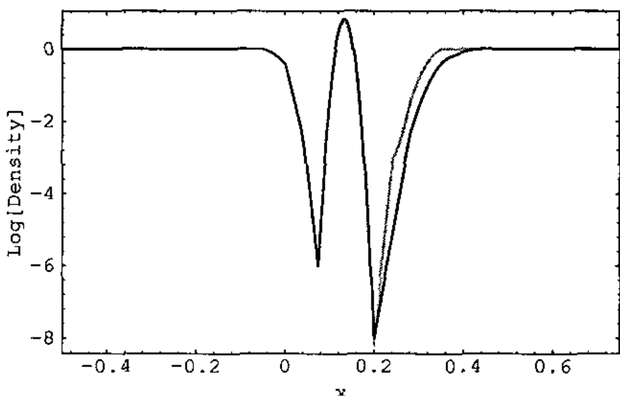

FIG. 7. Log[Density/10^{18} cm^{-3}] for $\Delta V = 0.205$ V.

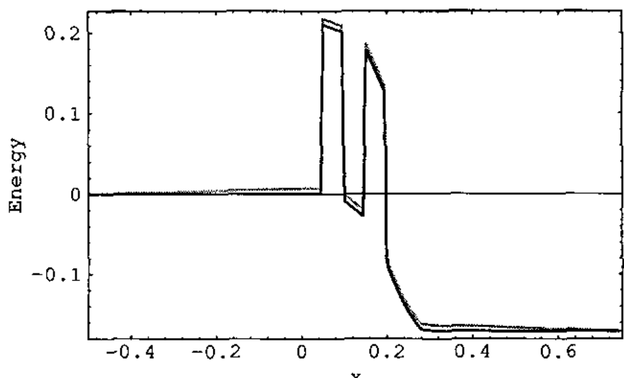

FIG. 9. Conduction band energy in eV for $\Delta V = 0.17$ V.

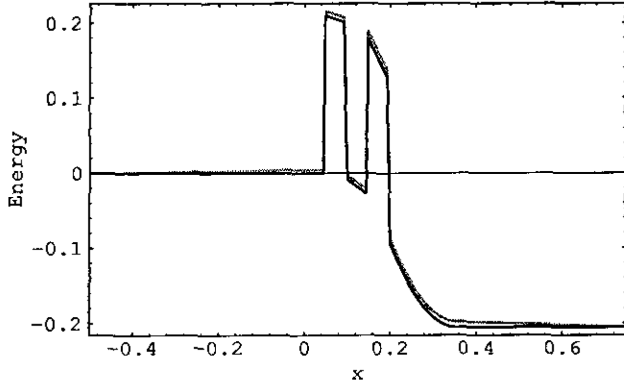

FIG. 10. Conduction band energy in eV for $\Delta V = 0.205$ V.

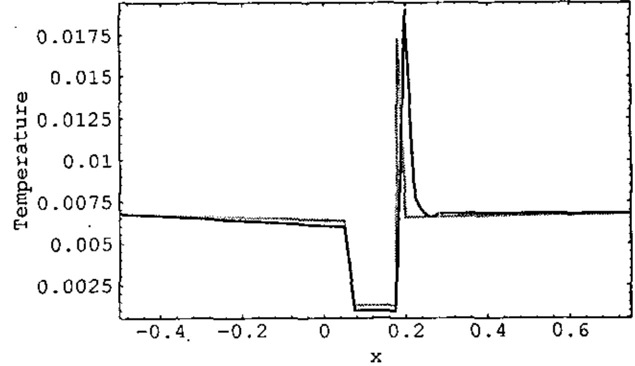

FIG. 12. Electron temperature in eV for $\Delta V = 0.17$ V.

$$\frac{\partial W_{cl}}{\partial t} + \frac{\partial}{\partial x_i}(u_i[W_{cl} + nT]) = -nu_i\frac{\partial V}{\partial x_i} - \frac{(W_{cl} - (3/2)\,nT_0)}{\tau w} + \nabla \cdot (\kappa \nabla T) + Q_W, \tag{13}$$

where W_{cl} is the classical energy density,

$$W_{cl} = \tfrac{3}{2}nT + \tfrac{1}{2}mnu^2, \tag{14}$$

Q is the quantum potential (see, e.g., [13]),

$$Q = -\frac{\hbar^2}{2m}\frac{1}{\sqrt{n}}\nabla^2\sqrt{n}, \tag{15}$$

and Q_W is given by

$$Q_W = \frac{\hbar^2 n}{24m\tau_w}\nabla^2\log(n) - \frac{\hbar^2}{24m}\nabla\cdot(n\nabla^2\mathbf{u}) - \frac{n}{3}\mathbf{u}\cdot\nabla Q. \tag{16}$$

The stress tensor is related to the quantum potential through the formula

$$-\frac{\partial}{\partial x_i}P_{ij} = \frac{\partial}{\partial x_j}(nT) + \frac{n}{3}\frac{\partial Q}{\partial x_j}. \tag{17}$$

If Q and Q_W are set to zero, Eqs. (11)–(13) are exactly the classical hydrodynamic transport equations.

Equations (11)–(13) can be written in conservation law form as

$$\frac{\partial \mathbf{w}}{\partial t} + \nabla\cdot\mathbf{F}(\mathbf{w}) = \mathbf{R}(\mathbf{w}), \tag{18}$$

where $\mathbf{w} = (n, mnu_x, mnu_y, mnu_z, W_{cl})^t$.

We will briefly describe the Runge–Kutta discontinuous Galerkin (RKDG) method for discretizing the left-hand side of Eq. (18) and then the mixed finite element method for discretizing Poisson's equation and the right-hand side of Eq. (18). Details for the classical hydrodynamic model are given in Ref. [7].

Suppose that Ω is the device domain and $\mathcal{T} = (0, t_{final})$ is the time interval of interest. First, let Π_h be a triangulation of Ω and set

$$V_h = \{\psi \in L^\infty(\Omega): \psi|_R \text{ is linear}, \forall R \in \Pi_h\}. \tag{19}$$

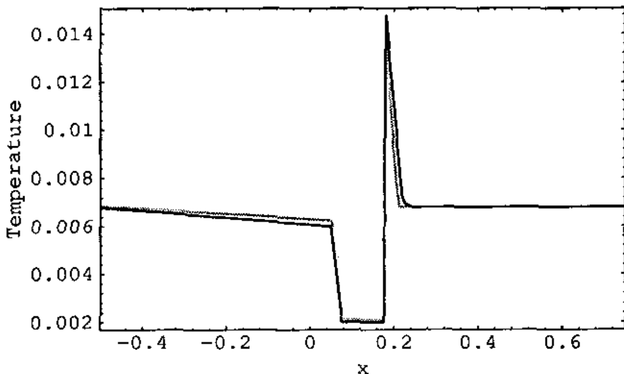

FIG. 11. Electron temperature in eV for $\Delta V = 0.135$ V.

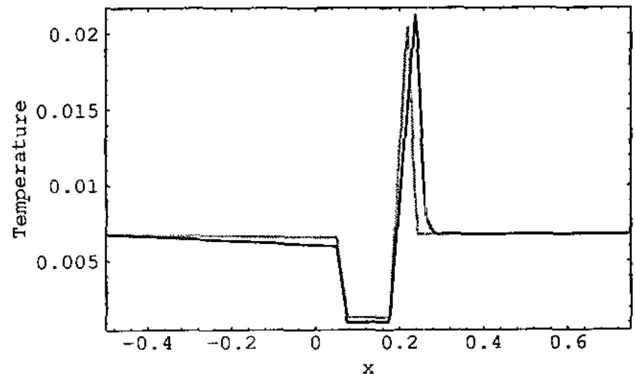

FIG. 13. Electron temperature in eV for $\Delta V = 0.205$ V.

Then for $t \in \mathcal{T}$, each of the components of the approximate solution $\mathbf{w}_h(t)$ is taken in V_h, and Eq. (18) is discretized in space using the discontinuous Galerkin method. The semi-discrete equations are written in the ODE form

$$\frac{d\mathbf{w}_h}{dt} = \mathbf{L}_h(\mathbf{w}_h) + \mathbf{R}_h(\mathbf{w}_h), \quad \mathbf{w}_h(t=0) = \mathbf{w}_{0h}, \qquad (20)$$

where each of the components of $\mathbf{w}_{0h}$ is taken to be the L^2-projection of the corresponding component of $\mathbf{w}_0$ onto V_h, and $\mathbf{L}_h$ is the approximation of $-\nabla \cdot \mathbf{F}$. Equation (20) gives an approximation $\mathbf{w}_h$ to $\mathbf{w}$ which is formally second-order accurate in space. The second-order accurate (in time) Runge–Kutta method is used to discretize the ODE (20). Finally, a local projection $\Lambda\Pi_h$ is applied to the intermediate values of the Runge–Kutta discretization to enforce nonlinear stability (through limiting the slope of the solution).

Let $\{(t_n, t_{n+1})\}_{n=0}^{N-1}$ be a partition of $\mathcal{T}$ into subintervals, and set $\Delta t_n = t_{n+1} - t_n$. Then the RKDG method is implemented in the following way:

1. Set $\mathbf{w}_h^0 = \Lambda\Pi_h(\mathbf{w}_{0h})$;
2. For $n = 0, \ldots, N-1$, compute $\mathbf{w}_h^{n+1}$:
   (i) Set $\mathbf{w}_h^{[0]} = \mathbf{w}_h^n$;
   (ii) Compute $\mathbf{w}_h^{[1]}$ and $\mathbf{w}_h^{[2]}$:
   $\mathbf{w}_h^{[1]} = \Lambda\Pi_h\,(\mathbf{w}_h^n + \Delta t_n \mathbf{L}_h\,(\mathbf{w}_h^{[0]}) + \Delta t_n \mathbf{R}_h\,(\mathbf{w}_h^{[0]}))$;
   $\mathbf{w}_h = \mathbf{w}_h^{[1]} + \Delta t_n \mathbf{L}_h\,(\mathbf{w}_h^{[1]}) + \Delta t_n \mathbf{R}_h(\mathbf{w}_h^{[1]})$;
   $\mathbf{w}_h^{[2]} = \Lambda\Pi_h\,(\tfrac{1}{2}(\mathbf{w}_h^n + \mathbf{w}_h))$;
   (iii) Set $\mathbf{w}_h^{n+1} = \mathbf{w}_h^{[2]}$.

The approximation operator $-\mathbf{L}_h$ and the local projection $\Lambda\Pi_h$ are described in Ref. [7].

To discretize Poisson's equation and the right-hand side of Eq. (18), we use the lowest-order Raviart–Thomas [14] mixed finite element method. We sketch out the details only for Poisson's equation,

$$\nabla \cdot \mathbf{E} = \frac{e}{\varepsilon}(N_D - N_A - n), \quad \mathbf{E} = -\nabla\phi \text{ in } \Omega \qquad (21)$$

with Dirichlet or Neumann boundary conditions

$$\phi = \phi_D \text{ on } \partial\Omega_D, \quad \mathbf{E}\cdot\mathbf{n} = 0 \text{ on } \partial\Omega_N. \qquad (22)$$

Here $\mathbf{n}$ is the outward pointing unit normal to $\partial\Omega$, $\partial\Omega = \partial\Omega_D \cup \partial\Omega_N$, and $\partial\Omega_D \cap \partial\Omega_N = \emptyset$.

The mixed finite element method discretization of Eqs. (21) and (22) gives the approximation $(\mathbf{E}_h, \phi_h) \in \mathbf{U}_h^\phi \times W_h$ as the solution of the weak formulation

$$(\nabla \cdot \mathbf{E}_h, \xi) = \left(\frac{e}{\varepsilon}(N_D - N_A - n_h), \xi\right), \forall \xi \in W_h \qquad (23)$$

$$(\mathbf{E}_h, \xi) - (\phi_h, \nabla\cdot\xi) = -\langle \phi_D, \xi\cdot\mathbf{n}\rangle_{\partial\Omega_D}, \quad \forall \xi \in U_h^\phi, \qquad (24)$$

where $(u, v) = \int_\Omega u\, v\, dx\, dy\, dz$, $\langle u, v\rangle_{\partial\Omega_D} = \int_{\partial\Omega_D} u(\gamma)\, v(\gamma)\, d\gamma$, n_h is the approximate density computed by the RKDG method, and $\mathbf{U}_h^\phi \times W_h$ is the lowest-order Raviart–Thomas mixed finite element space. This space over rectangular paralelepipeds is defined by

$$\mathbf{U}_h^\phi = \{\xi \in \mathbf{H}(\text{div}; \Omega): \xi|_R = (a_R^1 + a_R^2 x, a_R^3 + a_R^4 y, a_R^5 + a_R^6 z),$$
$$a_R^i \in \Re, \forall R \in \Pi_h; \xi\cdot\mathbf{n}|_{\partial\Omega_N} = 0\} \qquad (25)$$

$$W_h = \{\xi \in L^2(\Omega): \xi|_R \text{ is a constant}, \forall R \in \Pi_h\}. \qquad (26)$$

Finally, the approximation $\mathbf{E}_h$ is used to evaluate the terms in $\mathbf{R}$ in Eq. (18) that involve $\mathbf{E}$. The mixed finite element method gives the electric field in the precise form needed by the RKDG method and to a better approximation [14, 15] than more standard finite element and finite difference methods.

5. CONCLUSION

The existence of intrinsic bistability in the resonant tunneling diode has been confirmed through simulations of the quantum hydrodynamic model. The simulations demonstrate that the $O(\hbar^2)$ QHD equations reproduce important features of solutions to the full Wigner–Boltzmann equation.

Hysteresis appears in many settings in fluid dynamics, perhaps most spectacularly in Taylor–Couette flow. In this investigation, we have shown that hysteresis is manifested in the extension of classical fluid dynamics to quantum fluid dynamics. As in the classical case, bifurcation theory can be applied in analyzing the hysteresis points (see Ref. [16] for an analysis of Taylor–Couette hysteresis). In this analysis, the Lyapunov–Schmidt reduction can be applied analytically and numerically to the solutions near the hysteresis points.

In semiconductor device simulation, numerical methods must be robust over a wide parameter regime, due to the extreme variations in doping densities in typical devices. In addition, the left-hand side of the QHD equations (18) defines a nonlinear hyperbolic operator, and its hyperbolic modes permit the development of shock waves [17–20] in the classical hydrodynamic model. The novelty of our finite element method lies in the combination of the RKDG shock-capturing method for the nonlinear transport equations with a mixed finite element method for Poisson's equation and the right-hand side of Eq. (18). Since the RKDG/mixed finite element method works well for simulating both the classical and quantum hydrodynamic models, a single simulator can be used for modeling both standard and quantum devices.

REFERENCES

1. H. L. Grubin and J. P. Kreskovsky, *Solid-State Electron.* **32,** 1071 (1989).
2. C. L. Gardner, *SIAM J. Appl. Math.* **54,** 409 (1994).

3. C. L. Gardner, *VLSI Des.*, to appear.
4. N. C. Kluksdahl, A. M. Kriman, D. K. Ferry, and C. Ringhofer, *Phys. Rev. B* **39,** 7720 (1989).
5. W. R. Frensley, *J. Vacuum Sci. Technol. B* **3,** 1261 (1985).
6. V. J. Goldman, D. C. Tsui, and J. E. Cunningham, *Phys. Rev. Lett.* **58,** 1256 (1987); **59,** 1623 (1987).
7. Z. Chen, B. Cockburn, J. W. Jerome, and C.-W. Shu, *VLSI Des.*, to appear.
8. E. Wigner, *Phys. Rev.* **40,** 749 (1932).
9. M. G. Ancona and H. F. Tiersten, *Phys. Rev. B* **35,** 7959 (1987).
10. M. G. Ancona and G. J. Iafrate, *Phys. Rev. B* **39,** 9536 (1989).
11. H. Steinrueck and F. Odeh, *Z. Angew. Math. Phys.* **42,** 470 (1991).
12. M. Golubitsky and D. G. Schaeffer, *Singularities and Groups in Bifurcation Theory,* Vol. I (Springer-Verlag, New York, 1984).
13. C. Philippidis, D. Bohm, and R. D. Kaye, *Nuovo Cimento B* **71,** 75 (1982).
14. P. A. Raviart and J. M. Thomas, in *Mathematical Aspects of the Finite Element Method, Lecture Notes in Math.,* Vol. 606, 292 (Springer Verlag, Berlin, 1977).
15. Z. Chen, *RAIRO Modél. Math. Anal. Numér.* **27,** 9 (1993).
16. D. G. Schaeffer, *Math. Proc. Cambridge Philos. Soc.* **87,** 307 (1980).
17. C. L. Gardner, J. W. Jerome, and D. J. Rose, *IEEE Trans. Computer-Aided Des. Integrated Circuits Systems* **8,** 501 (1989).
18. C. L. Gardner, *IEEE Trans. Electron Devices* **38,** 392 (1991).
19. E. Fatemi, J. W. Jerome, and S. Osher, *IEEE Trans. Computer-Aided Des. Integrated Circuits Systems* **10,** 232 (1991).
20. C. L. Gardner, *IEEE Trans. Electron Devices* **40,** 455 (1993).